www.advmatinterfaces.de

Inherent Lattice Distortion Engineering via Magnetic Field for High-Quality Strained MAPbI₃ Perovskite Single Crystals

Abdulazeez M. Ogunleye, Hakseon Lee, Adeshina Mohammad Awwal, GunWoo Kim, Hyunmin Kim, Yoonmi Choi,* and Jonghoo Park*

Lattice distortion in perovskites (AMX₃) significantly impacts their stability and power conversion efficiency, often in a trade-off. The inherent lattice distortion is predominantly influenced by the size, orientation, and composition of the A-site cations. Notably, organic-inorganic hybrid lead halide perovskites with organic cations like methylammonium (MA) and formamidinium (FA) demonstrate high power conversion efficiency but compromised stability. Here, a novel synthesis method is presented for high-quality strained MAPbl₃ single crystals that offers not only enhanced optoelectronic properties but also improved thermal stability. This technique leverages the paramagnetic nature of the MA⁺ ion to manipulate lattice distortion. During the inverse temperature crystallization process, the dipole moment of the MA+ ion aligns with the direction of the external magnetic field. Correlating Fourier-transform infrared spectroscopy (FTIR) and X-ray diffraction (XRD) analysis demonstrates that this alignment, which induces compressive lattice strain, significantly enhances the carrier mobility from 68.1 to 487 cm² V s⁻¹, representing a sevenfold increase in hole mobility compared to the control sample. Additionally, it increases the carrier lifetime by 123%, from 23.458 to 52.364 ns, and improves thermal stability up to 230 °C. This findings reveal insights into the interplay between structural modifications and electronic properties, paving the way for tailored applications in photovoltaics, light-emitting devices, and beyond.

A. M. Ogunleye, H. Lee, G. Kim, J. Park School of Electronic and Electrical Engineering Kyungpook National University Daegu 41566, Republic of Korea E-mail: jonghoopark@knu.ac.kr

A. M. Awwal, H. Kim
Division of Biotechnology
Daegu Gyeongbuk Institute of Science and Technology (DGIST)
Daegu 42988, Republic of Korea

Y. Choi

Chemical Analysis Center Korea Research Institute of Chemical-Technology (KRICT) Daejeon 34 114, Republic of Korea

E-mail: ymchoi@krict.re.kr



© 2024 The Author(s). Advanced Materials Interfaces published by Wiley-VCH GmbH. This is an open access article under the terms of the Creative Commons Attribution License, which permits use, distribution and reproduction in any medium, provided the original work is properly cited.

DOI: 10.1002/admi.202400781

1. Introduction

In recent years, lead halide perovskites have emerged as highly promising materials for a wide range of applications, particularly in the field of photovoltaics, due to their exceptional optoelectronic properties.[1-5] These materials, with their generic formula AMX3, offer a high degree of compositional versatility, enabling significant tuning of material properties. However, this structural flexibility also poses challenges, particularly in terms of stability and efficiency of perovskite-based devices. The performance of lead halide perovskite materials is profoundly influenced by the choice of A-site cation.^[6,7] Inorganic cations like cesium (Cs) have shown promise, but the integration of organic cations such as MA and FA represents a significant breakthrough.[8,9] These organic-inorganic hybrid perovskites have demonstrated the ability to enhance the power conversion efficiency (PCE) of solar cells, rivaling or even surpassing the efficiency of other thin-film solar technologies. However, their inherent

instability under environmental stresses like humidity, temperature, and light exposure remains a significant challenge. The stability and efficiency of perovskite materials are strongly dependent on their crystallographic structure, with lattice distortion playing a critical role. [10,11] Various factors, such as the size, orientation, and chemical composition of the cations at the Asite of the perovskite lattice, can influence lattice distortion.[12–15] In addressing the challenges faced by organic-inorganic hybrid perovskites, researchers have turned their attention to controlling lattice distortions as a means to enhance both stability and efficiency. A wide range of techniques have emerged for distorting the octahedral structure, such as doping with other A-site cations, [16,17] applying external pressure, [18-20] exploring temperature effects, [18] and manipulating strain and lattice mismatch.[19,20] Specifically, in methylammonium lead iodide (MAPbI₃) perovskites, the orientation of the MA⁺ ion and its electric dipole moment creates a force field within the material, causing inherent distortion in the inorganic PbI₃ frame.^[9,21-23] The impact of lattice distortion extends beyond structural modifications; it also plays a pivotal role in influencing the charge



www.advancedsciencenews.com

ADVANCED MATERIALS INTERFACES

www.advmatinterfaces.de

carrier dynamics of perovskite single crystals. By altering the electronic band structure^[24] and affecting the magnetic behavior of these materials, lattice distortion significantly shapes their overall properties.^[25,26]

In this study, we introduce a novel synthesis method for highquality strained MAPbI₃ single crystals that not only enhances their optoelectronic properties but also improves stability. Our method involves engineering lattice distortion by leveraging the paramagnetic nature of the MA+ ion. During the inverse temperature crystallization (ITC) process, the magnetic dipole moment of the MA+ ion aligns with the external magnetic field, inducing controlled lattice distortion. ITC is a widely used technique for growing high-quality perovskite single crystals by decreasing the solubility of the precursor solution as temperature increases.[27-29] It produces high-purity crystals with controlled size and shape, ideal for optoelectronics and materials research. To evaluate the effectiveness of our approach, we conducted Xray Crystallography (XRC), XRD, and FTIR analyses. Through these analyses, we demonstrated that the alignment of MA+ ions impacts the lattice structure, inducing compressive strain. This structural modification, in turn, resulted in significantly improved optoelectronic properties and enhanced thermal stability. Specifically, we observed a remarkable sevenfold increase in hole mobility compared to the control sample, reaching a value of 487 cm² V s⁻¹, indicating improved charge transport. Additionally, we noted a 123% increase in carrier lifetime compared to crystals synthesized using the conventional ITC process, suggesting a reduction in recombination losses. Moreover, our method significantly improved the thermal stability of the crystals, allowing them to withstand temperatures up to 230 °C. The enhanced charge transport, reduced recombination losses, and high thermal stability in the strained perovskite single crystals can lead to significant improvements in efficiency and stability of various optoelectronic devices, including solar cells, LEDs, and photodetectors.

2. Results and Discussion

Our in-depth investigation into the paramagnetic properties of the MA⁺ ion was conducted using Gaussian DFT computations. We began by constructing a highly optimized molecular structure for the ion, providing a solid basis for our study. We deliberately select the B3LYP hybrid functional as our preferred exchange-correlation method, known for its accurate treatment of electron correlation and spin polarization, ensuring the reliability of our results. Utilizing spin-unrestricted calculations in our DFT software allowed us to model systems with unpaired electrons. These electrons, categorized as alpha (up) and beta (down) spin, occupy distinct spatial orbitals characterized by varying energies. In the context of a paramagnetic molecule hosting a lone unpaired electron, the resulting multiplicity manifests as a doublet, described by the equation Multiplicity = 2S + 1, where S represents the total spin number. Advancing through our computational analysis, we conclude our investigation by visually representing our findings using Gaussian as an external visualization tool. This representation elegantly illustrates the presence of the unpaired electron within the LUMO (0.084218 eV) of the ion, effectively exemplified in Figure S1 (Supporting Information).

The formation of MAPbI₃ from solid MAI and PbI₂ can be represented by the chemical equation:

Dissociation of reactants :
$$MAI \rightarrow MA^+ + I^-$$
 (1)

$$PbI_2 \to Pb^{2+} + 2I^-$$
 (2)

Formation of lead iodide complex :
$$Pb^{2+} + 2I^{-} \rightarrow PbI_{2}$$
 (3)

$$PbI_2 + I^- \to PbI_3^- \tag{4}$$

Formation of the perovskite structure : $MA^+ + PbI_3^- \rightarrow MAPbI_3$ (5)

Overall reaction : MAI + PbI₂
$$\rightarrow$$
 MA⁺ + 3I⁻ + Pb²⁺ \rightarrow MAPbI₃ (6)

During this reaction, the MA⁺ cation combines with the PbI₃ anion, [19,30] resulting in the creation of a 3D perovskite lattice structure. The Pb²⁺ cations occupy the octahedral sites formed by six iodide (I⁻) anions, while the MA⁺ cations occupy the larger cuboctahedra sites within the lattice. This forms a 3D network of corner-sharing PbI6 octahedral. This arrangement gives rise to the crystal structure of MAPbI₃, characterized by alternating layers of organic and inorganic components. By introducing a magnetic field during the synthesis process, an intriguing transformation occurs. The paramagnetic nature of the MA⁺ ions causes them to align with the direction of the magnetic field, as shown in Figure 1a. Figure 1b illustrates the crystalline structure of the MAPbI₃ perovskite, the final product of the magnetic fieldassisted ITC process. Within the PbI₆ octahedral framework, MA⁺ cations are interspersed, occupying interstitial sites and balancing the overall charge of the crystal. This precise arrangement ensures a well-ordered structure, contributing to the superior quality and performance of the MAPbI₃ perovskite. Figure 2a displays the XRD patterns of MAPbI3 single crystals, obtained using single crystal XRC rather than the conventional powder XRD. This technique provides precise information about atomic positions, bond angles, and distances, facilitating a detailed quantitative analysis of octahedral bond lengths and tilting distortions. Consequently, it allows for an accurate evaluation of lattice distortions and compressive strain, as depicted in Figure 2. The Xray diffraction (XRD) patterns reveal a prominent 110 peak, confirming the tetragonal phase in all the MAPbI₃ crystals.^[5] Interestingly, this peak position shifts systematically with increasing magnetic field strength. Specifically, the 110 peak occurs at $2\theta =$ 14.178° for the 0 T sample, shifting to $2\theta = 14.180$ and 14.186° for the 130 and 250 mT samples, respectively, as shown in the high-resolution XRD data in Figure S2a (Supporting Information). Similar trends are observed for other characteristic XRD peaks. The 220 peak shifts from $2\theta \approx 28.579^{\circ}$ at 0 T to 28.585 and 28.595° at 130 and 250 mT, respectively (Figure S2b, Supporting Information). Likewise, the 310 peak position changes from $2\theta \approx 32.037^{\circ}$ at 0 T to 32.044 and 32.056° at 130 and 250 mT (Figure S2c, Supporting Information). According to Bragg's law, the positions of diffraction peaks in an XRD pattern are determined by the interplanar spacing (d) and the angle of diffraction (θ), related by the equation 2d sin (θ) = $n\lambda$, where λ is the

21967350, 2025, 9, Downloaded from https://adv

onlinelibrary.wiley.com/doi/10.1002/admi.202400781 by Dægu Gyeongbuk Institute Of, Wiley Online Library on [08/05/2025]. See the Terms

s) on Wiley Online Library for rules of use; OA articles are governed by the applicable Creative Commons License

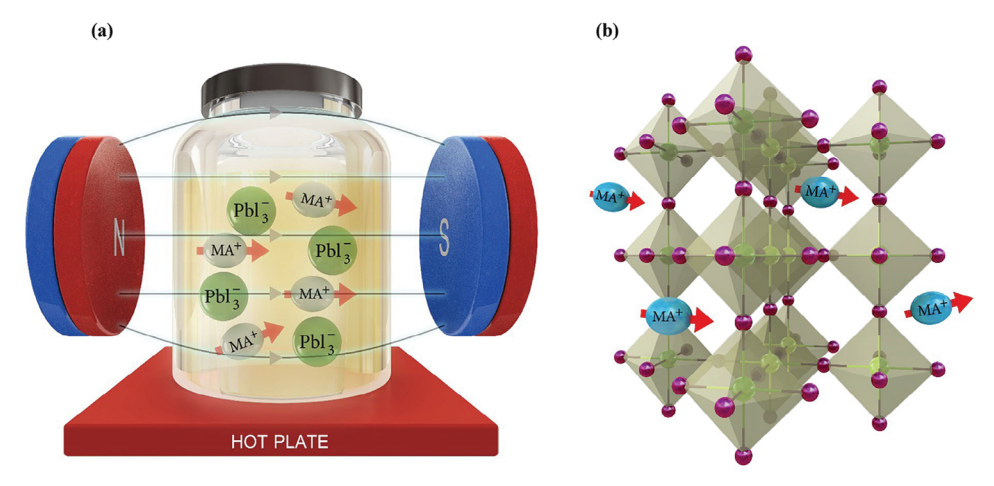


Figure 1. a) Graphical representation illustrating the alignment of the MA⁺ ion during magnetic field-assisted ITC. b) Crystal structure displaying the tetragonal phases of MAPbI₃ single crystals obtained via magnetic field-assisted ITC.

X-ray wavelength and n is an integer. As shown in Table S1 (Supporting Information), the interplanar spacing (d) decreases as the magnetic field increases. This reduction in d-value results in a shift of the diffraction peaks to higher angles (θ). The shift of XRD peaks to higher angles under magnetic fields directly reflects the magnetic field-induced compressive strain on the crystal lattice and the corresponding decrease in interplanar spacing within the MAPbI₂ samples. Compressive strains of $\approx 0.0215\%$ and 0.0555% are induced in the 130 and 250 mT crystals, respectively. The observed XRD peak shifts are attributed to compressive strain rather than a phase transition, as there are no changes in the space group due to the applied magnetic field, as shown in Table S5 (Supporting Information). Additionally, to precisely quantify the degree of distortion, we measured the Pb-I bond lengths and the I-Pb-I bond angles within the perovskite unit cell under varying magnetic field strengths using the single crystal XRD. For this purpose, we employed the distance distortion parameter (ϵ), which provides a quantitative assessment of the deviation of the octahedral bond lengths from their ideal values. This parameter allowed us to accurately evaluate the octahedral tilting distortions. We also calculated the tilting distortion parameter (Δ), which reflects the octahedral tilt of perovskites, and the I–I–I angle distortion index, [31,32] which indicates the average deviation of the I–I–I bond angles from the ideal angle of 90°. These parameters. [33,34] can be calculated as follows

$$\varepsilon = \sum_{i=1}^{6} |d_i - \langle d \rangle| \tag{7}$$

$$\Delta = \frac{1}{6} \sum_{i=1}^{6} \left(\frac{d_i - \langle d \rangle}{\langle d \rangle} \right)^2 \tag{8}$$

I – I – I angle distortion index =
$$\frac{\left(\Delta\theta_1 + \Delta\theta_2 + \Delta\theta_n\right)}{n}$$
 (9)

where d_i and $<\!d>$ represent the individual Pb–I interatomic distances and the average interatomic distance, respectively. Similarly, $\Delta\theta_1$, $\Delta\theta_2$, and $\Delta\theta_n$ denote the deviations of the I–I–I angles

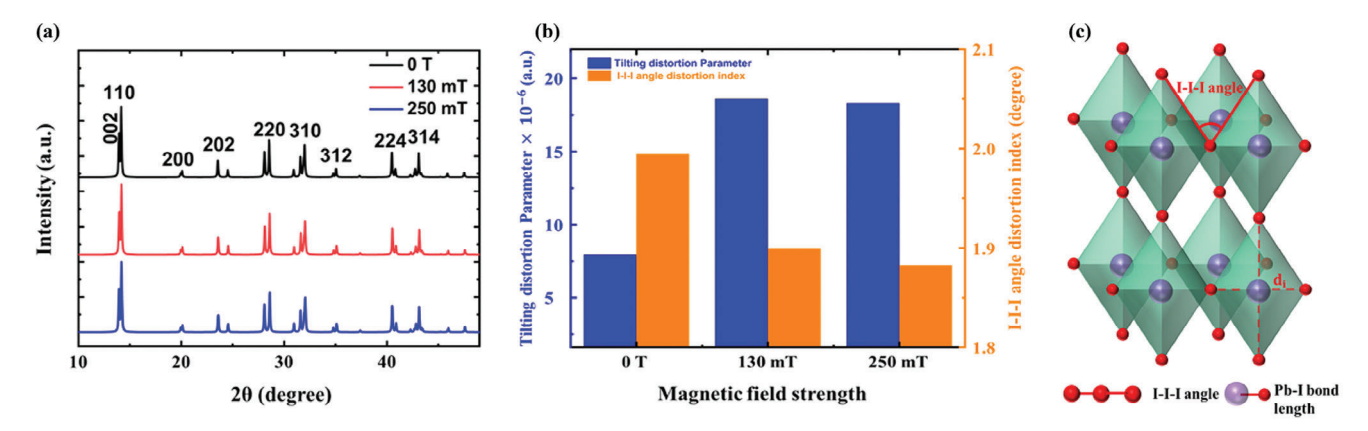


Figure 2. a) Single crystal X-ray diffraction (XRD) pattern of MAPbI₃ crystals grown with and without a magnetic field, simulated from single crystal X-ray crystallography (XRC). b) Bar chart showing the tilting distortion parameter (blue) and the I—I—I angle distortion index (orange) for MAPbI₃ single crystals grown at 0 T, 130 and 250 mT c) Key influenced geometric parameters of the MAPbI₃ crystals.

and-conditions) on Wiley Online Library for rules of use; OA articles are governed by the applicable Creative Commons

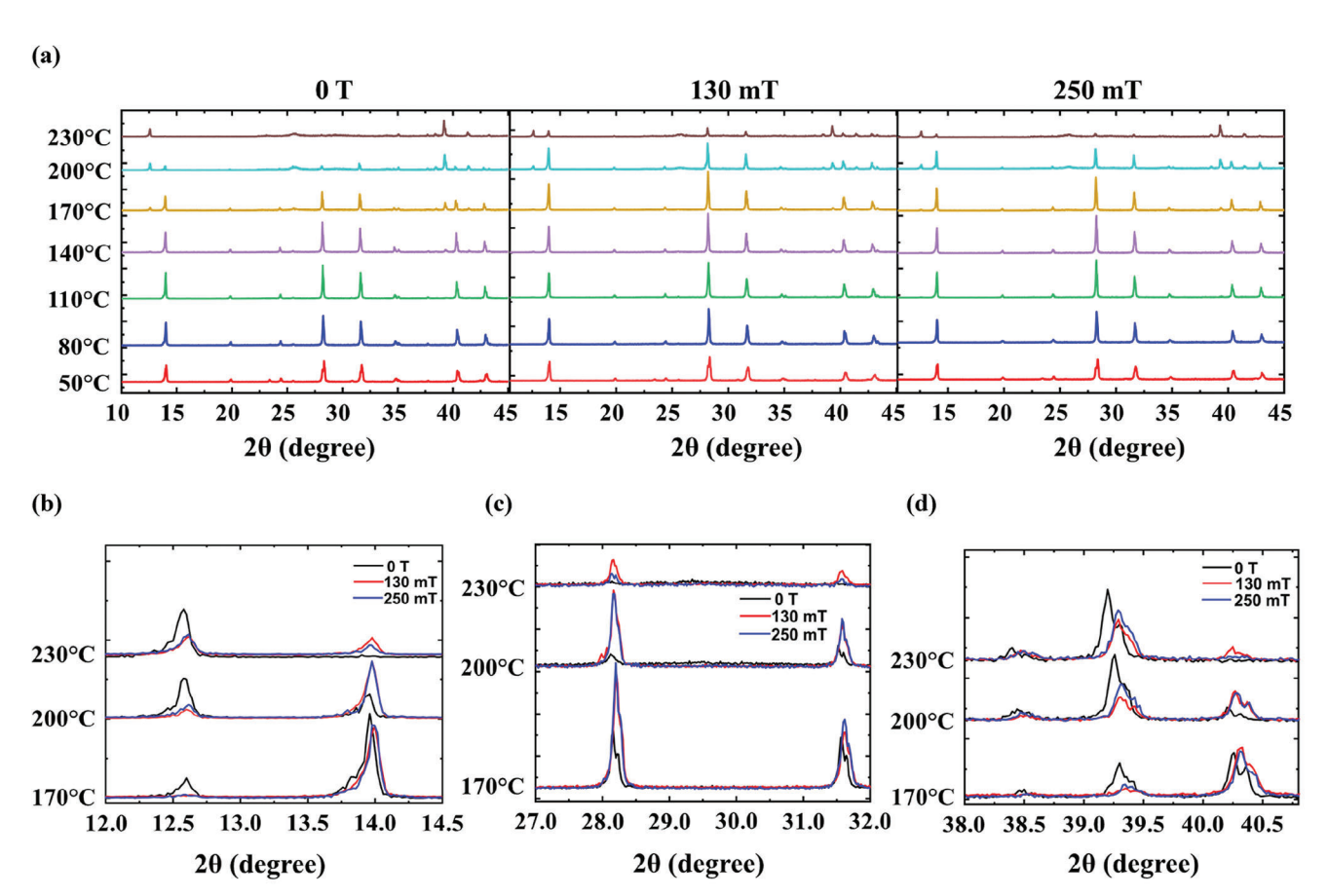


Figure 3. a) Temperature dependent XRD pattern of the magnetic field-assisted and control MAPbI₃ SCs. Enlarge XRD pattern at b) 12.0 to 14.5° c) 27.0 to 32.0° d) 38.0 to 41.0°.

from their ideal value of 90° for the three distinct iodine atoms within the crystal lattice.

Figure 2b,c illustrates the influence of magnetic field on the octahedral distortion parameter (ODP) and the I—I—I angle distortion index for MAPbI₃ single crystals. Our analysis reveals a strong correlation, where increasing the magnetic field leads to a higher ODP, indicating greater structural distortion within the crystal lattice. This, in turn, resulted in a lower degree of angular distortion between iodine atoms, further confirming the role of the magnetic field in modulating the lattice dynamics and inducing distortion within the MAPbI₃ crystal structure. This magnetic field-driven modulation of the crystal structure has important implications for optimizing the properties and functionality of MAPbI₃ for various optoelectronic applications.^[35,36]

The thermal stability of MAPbI $_3$ crystals grown with and without a magnetic field was studied using temperature-dependent X-ray diffraction (XRD). The XRD patterns of the perovskite single crystals at various temperatures (ranging from 50 to 230 °C) were analyzed as shown in **Figure 3a**. For the temperature up to 140 °C, all crystal samples showed distinct peaks at 2θ angles of 14.09, 19.96, 23.48, 24.47, 28.42, 31.77, 34.99, 40.43, 43.07, and 50.20°. These peaks corresponded to specific crystallographic planes, namely (110), (112), (211), (202), (220), (222), (312), (224), (314), and (404), confirming the presence of the MAPbI $_3$ tetragonal

phase, consistent with earlier studies.^[27,35] However, in the control crystals (0 T), at 170 °C, an impurity phase of PbI₂ (001), indicating thermal degradation, was detected with peaks observed at 12.6 and 39.2°. In contrast, the magnetic field-assisted crystals show no impurity phase at 12.6° and a weaker peak of 39.2° at 170 °C. At 230 °C, a stronger impurity phase of PbI₂ was detected at 12.6 and 39.2° in the control crystals, while the magnetic field-assisted crystals exhibited a weaker intensity of these impurity peaks as shown in Figure 3b,c. Furthermore, the characteristic perovskite peaks at 14.1, 28.3, and 40.43° completely disappeared in the control crystals at 230 °C, while the magnetic fieldassisted crystals retained their characteristic perovskite peaks, as shown in Figure 3b-d. The XRD analysis of the control crystal revealed a shift in the diffraction peak of PbI₂ (110) plane toward a lower angle as the temperature increased, indicating an increase in interatomic spacing and broader plane space. This change in spacing suggests potential decomposition of the crystals, making them less stable at higher temperatures. These findings demonstrate that the magnetic field-assisted crystals exhibit higher thermal stability and resistance to degradation compared to the control crystals, which experienced changes in their crystal structure at elevated temperatures. The incorporation of a magnetic field during crystal growth has proven beneficial in preserving the integrity of the perovskite crystal structure under high-temperature conditions. This enhanced thermal stability holds great promise

www.advancedsciencenews.com



www.advmatinterfaces.de

(b) O T 130 mT 250 mT Absorbance (a.u.)

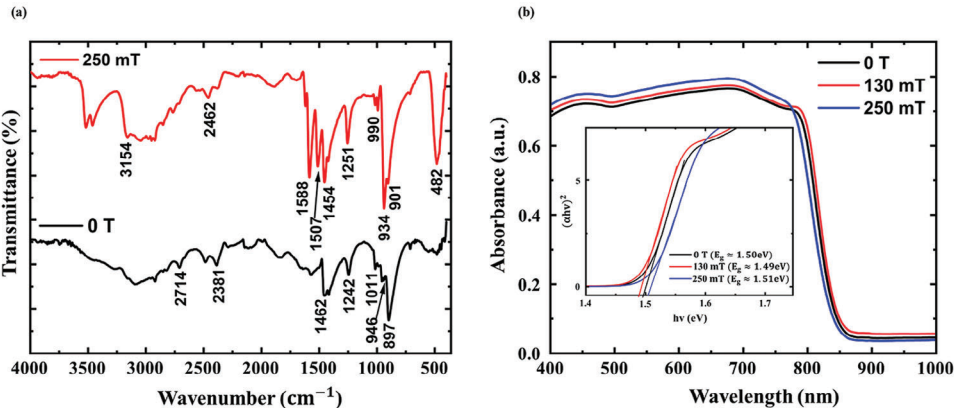


Figure 4. a) FT-IR spectra of the magnetic field-assisted and control MAPbl₃ SCs. b) UV-vis absorption spectra, the inset is bandgap calculation with a Tauc plot.

for advancing the applications of perovskite materials in various

Figure 4a shows a comparison of the FTIR spectra of the magnetic field-assisted crystals (250 mT) and control crystals (0 T). The FTIR spectrum offers valuable information about the chemical components and the octahedral stretching present in the magnetic-assisted crystals. In the magnetic field-assisted crystal, a stronger IR vibrational mode appears at 482 cm⁻¹. This mode corresponds to the stretching vibration of the metaloxygen (M-O) bond, specifically the Pb-I bonds in this case.[36] The observation confirms that the magnetic field induces strain on the crystal, leading to alterations in the Pb-I bonding.[19] At 901 cm⁻¹, the IR vibrational mode corresponds to the CH₃-NH₃⁺ rocking vibration of the magnetic field-assisted MAPbI3, while a similar vibration is observed at 897 cm⁻¹ for the control crystal. This suggests that the magnetic field affects the CH₃-NH₃+ rocking vibration, possibly altering the molecular arrangement and dynamics. The sharp peaks at 1242 and 1251 cm⁻¹ represent the C-N stretching vibrations of the MA group present in both crystals, suggesting changes in the molecular conformation and interactions of the MA+ cations. Other band assignments are detailed in Table S2 (Supporting Information). The acquired results are in good agreement with the values reported previously.[27,37] These MA+ ions exhibit paramagnetism due to their unpaired electrons, resulting in individual magnetic moments that interact with external magnetic fields. When a magnetic field is present, the paramagnetic MA⁺ ions tend to align with the direction of the magnetic field. This alignment significantly impacts the overall molecular motion of the ions. Figure 4b displays the UV-vis absorption spectra of both the magnetic field-assisted crystals and the control crystal. Inset shows a direct bandgap Tauc plot to analyze the absorption spectra. The fitting yielded bandgap of ≈1.49 and 1.51 eV for the magnetic field-assisted crystals with magnetic fields of 130 and 250 mT, respectively, which are similar to that of the control crystal, 1.50 eV. Figure \$4 (Supporting Information) presents the photoluminescence (PL) spectra of the magnetic field-assisted crystals. The photoluminescence (PL) spectra of crystals grown with magnetic field of 130 and 250 mT exhibit full width at half maximum (FWHM) values of 48.3 and 47.8 nm, respectively. In comparison, the FWHM for control crystal is 49.5 nm. This indicates that the 250 mT magnetic field-assisted crystal is 1.7 nm narrower than the control crystal. The narrower FWHM in the PL spectra of the magnetic field-assisted crystals suggests well-ordered crystalline structures and a low defect density. To investigate the effect of the magnetic field on the carrier transport process, nanosecond transient photoluminescence (PL) spectroscopy was employed. The PL spectroscopy revealed two distinct time components in the decay process, referred to as the fast decay (τ_1) and the slower component (τ_2) , as depicted in **Figure 5**a.

These two components were associated with surface defects and carrier recombination in the bulk, respectively.^[8] Both the surface carrier constants (related to the fast component) and the bulk carrier constants (related to the slow component) were found to be sensitive to the magnetic field. The obtained time constants (τ) for the fast component were 1.072 \pm 0.203 ns for the control samples (0 T), 1.217 ± 0.238 ns for the magnetic field of 130 mT, and 3.947 ± 0.382 ns for the magnetic field of 250 mT. Similarly, the time constants for the slow component were 23.458 \pm 3.034 ns for the control samples (0 T), 35.030 \pm 6.030 ns for the magnetic field of 130 mT, and 52.364 ± 3.090 ns for the magnetic field of 250 mT. This suggests that the presence of the magnetic field influenced the charge carrier dynamics, resulting in a slower decay of the carriers in the magnetic fieldassisted crystals. Specifically, the carrier lifetime was ≈ 3 times longer for the magnetic field-assisted crystals. This enhanced carrier lifetime suggests improved carrier recombination dynamics and reduced surface defects in the magnetic field-assisted crystals, which can contribute to enhanced optoelectronic performance and efficiency in potential applications. We conducted Hall Effect measurements to investigate the charge carrier behaviors of three different MAPbI₃ samples (0 T, 130, and 250 mT) at room temperature. The mobility values obtained are as follows: $69.1 \text{ cm}^2 \text{ s}^{-1} \text{ V}^{-1}$ for the 0 T sample, $114 \text{ cm}^2 \text{ s}^{-1} \text{ V}^{-1}$ for the 130 mT sample, and an impressive 487 cm² s⁻¹ V⁻¹ for the 250 mT sample as outlined in Table S4 (Supporting Information). This sevenfold increase in hole mobility compared to the control sample highlights the profound influence of magnetic fieldassisted growth on charge carrier transport in perovskite single crystals. When benchmarked against other reported MAPbI3 single crystals, measured using both Hall and space charge limit current (SCLC) methods,[38-40] the magnetic field-assisted samples

www.advancedsciencenews.com

ADVANCED
MATERIALS
INTERFACES

www.advmatinterfaces.de

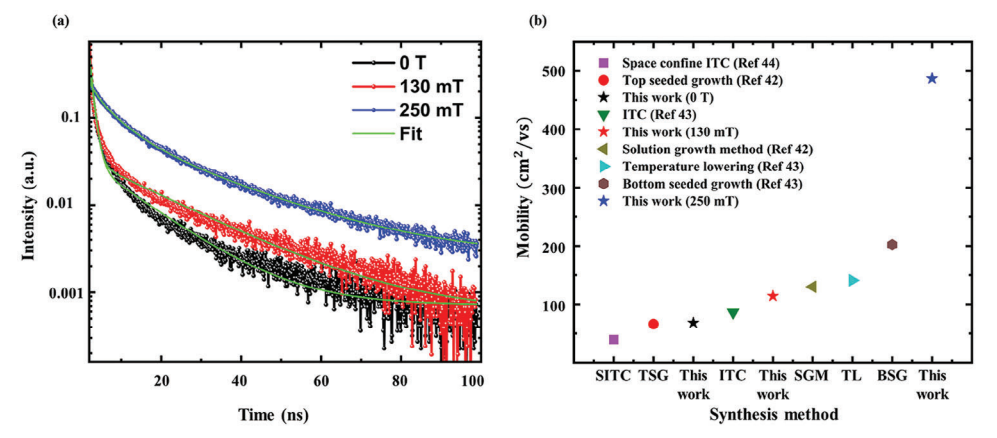


Figure 5. a) Time-resolved PL (TRPL) decay spectra of MAPbI₃ single crystals obtain without magnetic field and under magnetic field. b) Performance graph of reported carrier mobility in MAPbI₃ single crystals.

presented in this work exhibit the highest hole mobility values documented to date, as illustrated in Figure 5b. This substantial increase in hole mobility indicates that the magnetic field-assisted crystals have a higher capacity for efficient charge carrier transport, leading to improved electronic properties.

3. Conclusion

In conclusion, we present a novel synthesis method designed to enhance both the optoelectronic properties and stability of MAPbI₂ single crystals. This approach exploits the paramagnetic characteristics of the MA⁺ ion, specifically by its alignment with an external magnetic field during the ITC process. The octahedral distortion, evident in FTIR, XRC, and XRD analyses, is attributed to the alignment of MA+ ions within the crystal lattice under the influence of the magnetic field. This strategic manipulation of lattice distortion significantly improves the material's performance characteristics. The strained MAPbI3 single crystals demonstrated a remarkable 123% increase in the slow time component of hole mobility compared to control samples. While the control crystals exhibited a hole mobility of 68.1 cm² s⁻¹ V⁻¹, the magnetic field-assisted crystals showed a substantial sevenfold rise to 487 cm 2 s $^{-1}$ V $^{-1}$. This extended slow time component and elevated hole mobility in the magnetically-treated crystals indicate enhanced charge carrier transport and reduced recombination losses. These findings suggest that leveraging magnetic fields can be an effective strategy for optimizing the charge dynamics within perovskite single crystals. Not only did our method elevate the optoelectronic properties of the crystal, but it also significantly improved its thermal stability. The engineered lattice distortion allowed the crystals to withstand temperatures up to 230 °C without any signs of deterioration. This newfound stability not only enhances the reliability of devices but also opens up exciting opportunities for applications in high-temperature environments.

Our findings highlight the potential of magnetic field-assisted growth as a promising technique for synthesizing high-quality strained perovskite single crystals. This method opens up new possibilities for enhancing the performance of perovskite-based optoelectronic devices, such as high-efficiency solar cells, LEDs, and photodetectors. Future research could delve deeper into un-

derstanding the underlying mechanisms of crystal growth under a magnetic field and explore the applicability of this technique to other perovskite materials, paving the way for further advancements in the field of perovskite-based devices.

4. Experimental Section

Chemicals: Lead iodide (PbI₂, 99.999% trace metal basis), Gamma-butyrolactone (GBL) (Z99%) were purchased from Sigma Aldrich. Methylammonium iodide (MAI) were purchased from Dyesol Limited (Australia). All salts and solvents were used as received without any further purification.

Synthesis of MAPbl₃ Single Crystal: MAPbl₃ single crystals were grown by the inverse temperature crystallization method with and without the assistance of an external magnetic field. 1.5 M of MAPbl₃ in GBL was prepared by dissolving an equimolar amount of MAI and Pbl₂ in GBL at 65 °C by stirring overnight to a mostly clear, homogeneous solution. The solutions were filtered using a PTFE filter with 0.2 mm pore size. One millilitres of the filtrate were placed in a vial and the vial was kept in an oil bath undisturbed. The temperature was gradually increased to 110 °C and maintained for 6 h. In the magnetic field-assisted experiments, a magnetic field with a strength of 130 and 250 mT was applied during the entire growth process. The resulting crystals were then washed with GBL and dried at a temperature of 65 °C for 12 h.

Characterization: The measurement of single crystal XRC was carried out using a Rigaku/XtaLAB Synergy, MoKlpha ($\lambda=0.71073~{
m \AA}$). X-ray diffractometer at a temperature of 223 K. The temperature-dependent XRD data was collected using a Rigaku Ultima IV X-ray diffractometer with Cu Kα radiation ($\lambda = 1.5418$ Å). The temperature dependence XRD was carried out using a Rigaku Ultima IV X-ray Diffractometer (XRD) with Cu Kα radiation ($\lambda = 1.5418 \text{ Å}$) at 40 kV and 40 mA, employing the High Temperature XRD (HTXRD) method. The absorbance spectra measurements were performed using UV-vis spectrometer (Perkin Elmer Lambda 950). Timeresolved photoluminescence (TRPL) measurement study was carried out using a confocal microscope (MicroTime-200, Picoquant, Germany) with a 10× (air) objective. For the lifetime measurements, a single-mode pulsed diode laser (470 nm with a pulse width of \approx 30 ps and an average power of 30-100 nW operating in 1 MHz repetition rate) was used as an excitation source. A dichroic mirror (490 DCXR, AHF), a long-pass filter (HQ500lp, AHF), a 150 µm pinhole, a bandpass filter (500-600 nm, Thorlabs), and a single photon avalanche diode (PDM series, MPD) were used to collect emission from the samples. A time-correlated single-photon counting system (PicoHarp-300, PicoQuant GmbH) was used to count emission photons. Exponential function fittings for the obtained PL decays were performed using Symphotime-64 software (Ver. 2.2). The Hall mobility and Carrier trap density measurements were carried out with the Ecopia

ADVANCED SCIENCE NEWS

www.advancedsciencenews.com

www.advmatinterfaces.de

HMS3000 system (magnetic field of 0.51 T), using the Van der Pauw hall effect measurement technique at room temperature.

Supporting Information

Supporting Information is available from the Wiley Online Library or from the author.

Acknowledgements

This work was supported by the National Research Foundation of Korea (NRF) grant funded by the Korean government (MSIT) [NRF-2023R1A2C1007997] and the Korea Research Institute of Chemical Technology (KRICT) through a project No KK2452-10.

Conflict of Interest

The authors declare no conflict of interest.

Data Availability Statement

The data that support the findings of this study are available in the supplementary material of this article.

Keywords

magnetic field-assisted ITC, octahedral distortion, perovskite single crystals, strained perovskite, thermal stability

Received: September 29, 2024 Revised: November 6, 2024 Published online: November 24, 2024

- M. Degani, Q. An, M. Albaladejo-Siguan, Y. J. Hofstetter, C. Cho, F. Paulus, G. Grancini, Y. Vaynzof, Sci. Adv 2021, 7, 7930.
- [2] H. E Dong, C. Ran, W. Gao, M. Li, Y. Xia, W. Huang, eLight 2023, 3, 3.
- [3] N. Arora, M. I. Dar, A. Hinderhofer, N. Pellet, F. Schreiber, S. M. Zakeeruddin, M. Grätzel, *Science* 2017, 358, 768.
- [4] A. Al-Ashouri, E. Köhnen, B. Li, A. Magomedov, H. Hempel, P. Caprioglio, J. A. Márquez, A. B. M. Vilches, E. Kasparavicius, J. A. Smith, N. Phung, D. Menzel, M. Grischek, L. Kegelmann, D. Skroblin, C. Gollwitzer, T. Malinauskas, M. Jošt, G. Matič, B. Rech, R. Schlatmann, M. Topič, L. Korte, A. Abate, B. Stannowski, D. Neher, M. Stolterfoht, T. Unold, V. Getautis, S. Albrecht, *Science* 2020, 370, 1300.
- [5] S. Kavadiya, J. Strzalka, D. M. Niedzwiedzki, P. Biswas, J. Mater. Chem. A 2019, 7, 12790.
- [6] D. Bi, W. Tress, M. I. Dar, P. Gao, J. Luo, C. Renevier, K. Schenk, A. Abate, F. Giordano, J.-P. Correa Baena, J.-D. Decoppet, S. M. Zakeeruddin, M. K. Nazeeruddin, M. Grätzel, A. Hagfeldt, Sci. Adv. 2016, 2, 1501170.
- [7] D. P. Mcmeekin, G. Sadoughi, W. Rehman, G. E. Eperon, M. Saliba, M. T. Hörantner, A. Haghighirad, N. Sakai, L. Korte, B. Rech, M. B. Johnston, L. M. Herz, H. J. Snaith, *Science* 2016, 351, 151.
- [8] C. C. Stoumpos, C. D. Malliakas, M. G. Kanatzidis, *Inorg. Chem.* 2013, 52, 9019.
- [9] A. Amat, E. Mosconi, E. Ronca, C. Quarti, P. Umari, M. K. Nazeeruddin, M. Grätzel, F. De Angelis, Nano Lett. 2014, 14, 3608.

- [10] D. J. Fairfield, H. Sai, A. Narayanan, J. V. Passarelli, M. Chen, J. Palasz, L. C. Palmer, M. R. Wasielewski, S. I. Stupp, J. Mater. Chem. A 2019, 7 1687
- [11] H. Bi, M. Wang, L. Liu, J. Yan, R. Zeng, Z. Xu, J. Wang, J. Mater. Chem. A 2024, 12, 12744.
- [12] S. Liu, J. Wang, Z. Hu, Z. Duan, H. Zhang, W. Zhang, R. Guo, F. Xie, Sci Rep 2021, 11, 20433.
- [13] J. Hu, J. Wang, H. Chen, X. Niu, npj Comput. Mater. 2024, 10, 140.
- [14] H. S. Kim, N. G. Park, NPG Asia Mater. 2020, 12, 78.
- [15] P. R. Varadwaj, A. Varadwaj, H. M. Marques, K. Yamashita, Sci. Rep. 2019, 9, 50.
- [16] R. Prasanna, A. Gold-Parker, T. Leijtens, B. Conings, A. Babayigit, H.-G. Boyen, M. F. Toney, M. D. McGehee, J. Am. Chem. Soc. 2017, 139, 11117.
- [17] P. Bhatt, A. Kumar, N. Singh, A. Garg, K. S. Nalwa, A. Tewari, ACS Appl. Energy Mater. 2023, 6, 6615.
- [18] Ardimas, T. Pakornchote, W. Sukmas, S. Chatraphorn, S. J. Clark, T. Bovornratanaraks, Sci Rep 2023, 13, 16854.
- [19] J. Fowlie, C. Lichtensteiger, M. Gibert, H. Meley, P. Willmott, J.-M. Triscone, Nano Lett. 2019, 19, 4188.
- [20] J. Wu, J. Wu, S. Liu, Z. Li, S. Wang, D. Xue, Y. Lin, J. Hu, Natl. Sci. Rev. 2018, 8, 2021.
- [21] T. Baikie, N. S. Barrow, Y. Fang, P. J. Keenan, P. R. Slater, R. O. Piltz, M. Gutmann, S. G. Mhaisalkar, T. J. White, J. Mater. Chem. A 2015, 3, 9298.
- [22] F. Zheng, H. Takenaka, F. Wang, N. Z. Koocher, A. M. Rappe, J. Phys. Chem. Lett. 2015, 6, 31.
- [23] J. Ma, L. W. Wang, Nano Lett. 2015, 15, 248.
- [24] E. I. Marchenko, V. V. Korolev, S. A. Fateev, A. Mitrofanov, N. N. Eremin, E. A. Goodilin, A. B. Tarasov, Chem. Mater. 2021, 33, 7518.
- [25] V. A. Bokov, N. A. Grigoryan, M. F. Bryzhina, V. V. Tikhonov, Phys. Status Solidi B 1968, 28, 835.
- [26] B.-Q. Zhao, Y. Li, X.-Y. Chen, Y. Han, S-H. Wei, K. Wu, X. Zhang, Adv. Sci. 2023, 10, 202300386.
- [27] M. I. Saidaminov, A. L. Abdelhady, B. Murali, E. Alarousu, V. M. Burlakov, W. Peng, I. Dursun, L. Wang, Y. He, G. Maculan, A. Goriely, T. Wu, O. F. Mohammed, O. M. Bakr, *Nat. Commun.* 2015, 6, 7586
- [28] G. Maculan, A. D. Sheikh, A. L. Abdelhady, M. I. Saidaminov, M. A. Haque, B. Murali, E. Alarousu, O. F. Mohammed, T. Wu, O. M. Bakr, J. Phys. Chem. Lett. 2015, 6, 3781.
- [29] R. K. Battula, G. Veerappan, P. Bhyrappa, C. Sudakar, E. Ramasamy, Surf. Interfaces 2023, 36, 102475.
- [30] Y. Ma, P. M. Hangoma, W. I. Park, J. H. Lim, Y. K. Jung, J. H. Jeong, S. H. Park, K. H. Kim, *Nanoscale* 2019, 11, 170.
- [31] L. Fan, S. Hao, S. He, X. Zhang, M. Li, C. Wolverton, J. Zhao, Q. Liu, Dalton Trans. 2023, 52, 5119.
- [32] M. Yao, M. Yao, Y. Zhang, J. Ban, J. Hou, B. Zhang, J. Liu, X. Ming, X. Kuang, Phys. Chem., Chem. Phys. 2023, 25, 19158.
- [33] M. O. B Yusuf, Appl. Sci. 2023, 13, 3353.
- [34] G. Bakradze, A. Kuzmin, Mater. 2022, 15, 7619.
- [35] C. A. López, C. Abia, J. E. Rodrigues, F. Serrano-Sánchez, N. M. Nemes, J. L. Martínez, M. T. Fernandez-Díaz, N. Biškup, C. Alvarez-Galván, F. Carrascoso, A. Castellanos-Gomez, J. A. Alonso, *Sci Rep* 2020, 10, 11228.
- [36] N. Sivakumar, S. Saha, R. Madaka, N. Bandaru, J. K. Rath, J. Mater. Sci.: Mater. Electron. 2023, 34, 1193.
- [37] X. Li, X. Li, W. Zhang, Y. Wang, W. Zhang, H. Wang, J. Fang, Nat. Commun. 2018, 9, 3806.
- [38] R. Dong, Y. Fang, J. Chae, J. Dai, Z. Xiao, Q. Dong, Y. Yuan, A. Centrone, X. C. Zeng, J. Huang, Adv. Mater. 2015, 27, 1912.
- [39] Z. Lian, Q. Yan, T. Gao, J. Ding, Q. Lv, C. Ning, Q. Li, J.-L. Sun, J. Am. Chem. Soc. 2016, 138, 9409.
- [40] Y. Liu, Y. Zhang, Z. Yang, D. Yang, X. Ren, L. Pang, S. (.F.). Liu, Adv. Mater. 2016, 28, 9204.